Force modulation and electrochemical gating of conductance in a cytochrome

2008 J. Phys.: Condens. Matter 20 374123

(http://iopscience.iop.org/0953-8984/20/37/374123)

IOP Publishing Journal of Physics: Condensed Matter

J. Phys.: Condens. Matter **20** (2008) 374123 (9pp) doi:10.1088/0953-8984/20/37/374123

Force modulation and electrochemical gating of conductance in a cytochrome

Jason J Davis, Ben Peters and Wang Xi

Chemistry Research Laboratory, University of Oxford, Mansfield Road, Oxford OX1 3TA, UK

E-mail: jason.davis@chem.ox.ac.uk

Received 22 February 2008, in final form 5 May 2008
Published 26 August 2008
Online at stacks.iop.org/JPhysCM/20/374123

Abstract

Scanning probe methods have been used to measure the effect of electrochemical potential and applied force on the tunnelling conductance of the redox metalloprotein yeast iso-1-cytochrome c (YCC) at a molecular level. The interaction of a proximal probe with any sample under test will, at this scale, be inherently perturbative. This is demonstrated with conductive probe atomic force microscopy (CP-AFM) current–voltage spectroscopy in which YCC, chemically adsorbed onto pristine Au(111) via its surface cysteine residue, is observed to become increasingly compressed as applied load is increased, with concomitant decrease in junction resistance. Electrical contact at minimal perturbation, where probe–molecule coupling is comparable to that in scanning tunnelling microscopy, brings with it the observation of negative differential resistance, assigned to redox-assisted probe–substrate tunnelling. The role of the redox centre in conductance is also resolved in electrochemical scanning tunnelling microscopy assays where molecular conductance is electrochemically gateable through more than an order of magnitude.

(Some figures in this article are in colour only in the electronic version)

1. Introduction

Scanning probe microscopes offer a convenient method of creating metal–molecule–metal junctions with a high degree of spatial and load control over the molecular configuration under analysis. Scanning tunnelling microscopy (STM) enables routine imaging of single molecules with lateral resolution at the ångström level while a conductive probe atomic force microscope (CP-AFM) decouples electronic effects from mechanical, providing controllable applied load with simultaneous conductance measurement and current–voltage spectroscopy. The STM environment can be modified such that the substrate is kept under full electrochemical control. By coupling appropriate tip insulation with the use of a bipotentiostat the biased tunnelling electrodes may be locked to an absolute potential scale. Such a configuration enables electrochemical gating and a resolution of redox site transconductance.

In the current work, an analysis of the tunnelling properties of the protein cytochrome c has been carried out using both CP-AFM and EC-STM. Cytochromes c are a family of redox-active proteins that act as electron shuttles in the respiratory chain; redox-activity arises from the presence of a heme group and its associated Fe(II)/Fe(III) switch. In order to probe the properties of a structurally complex macromolecule, it is highly advantageous to interface with electrodes in a robust and molecularly-ordered manner. In previous work we have established protocols for metalloprotein immobilization through naturally expressed or engineered solution-exposed cysteines [1–4]. *Saccharomyces cerevisiae* yeast iso-1-cytochrome c (YCC) has a natural surface cysteine residue Cys102 that can be used to bind the protein to a gold substrate. Recent work has established that this residue can be used to from redox-addressable monolayers [5–8]. In order to clarify the role of the redox centre, a comparable redox-inactive protein was analysed under equivalent conditions. Zn-azurin is of similar dimensions to YCC and also forms layers suitable for scanning probe studies (as determined here by STM imaging, data not shown, and previously [3, 4, 9]), robustly chemisorbing to gold via a solution-exposed disulphide moiety. The use of Zn-porphyrin cytochrome c was not utilized due to the destabilizing effect of the zinc metal centre [10], so Zn-azurin is considered to be a suitable control. In the following work we have used CP-AFM to both measure molecular conductance and demonstrate the importance of probe-induced molecular perturbation in subsequently assayed junction properties. EC-STM has been used to demonstrate gated molecular conductance in the redox protein. In a

comparative study with horse-heart cytochrome c (HHCC) we have looked at the effect of a 'spacing' monolayer [7] on electrode–protein coupling and the effect this subsequently has on the magnitude of conductance gating.

1.1. Electronic transport theoretical analyses

We have previously shown that, in the absence of resonant conditions, a protein molecule can be treated as a structureless dielectric in the Simmons tunnelling model [4, 11]. This can be used to estimate the barrier height ϕ and length L presented to the electrons as they tunnel through a monolayer, and also the asymmetry factor α (a measure of the different potential shifts at tip and substrate). Originally developed by John Simmons in 1963 [12], the formulation relates current density i to the applied bias for idealized metal–insulator–metal devices according to:

$$i = \frac{e^2}{2\pi h L^2}\left\{(\phi_0 - \alpha V)\exp(-K(\phi_0 - \alpha V)^{\frac{1}{2}}) - (\phi_0 + (1-\alpha)V)\exp(-K(\phi_0 + (1-\alpha)V)^{\frac{1}{2}})\right\} \quad (1)$$

where

$$K = \frac{4\pi L}{h}(2me)^{1/2} \quad (2)$$

where e is the electronic charge, h is Planck's constant, L is the tunnelling distance, V the applied bias, m is the effective electron mass, ϕ is the barrier height and h is Planck's constant. This formulation is valid for the 'medium-voltage' regime where $V < \phi_0/e$. In this direct tunnelling model the barrier is regular and featureless, spanning the space between both electrodes which have electronic density of state (DOS) distributions described by the Fermi function at absolute zero, i.e. a step function. In the presence of an accessible redox centre this model may not be accurate. At certain electron energies the redox site may be populated by tunnelling electrons. The possibility of such residency may effectively present a preferential pathway for the electrons, enhancing the transmission probability at specific bias. This situation is known as 'two-step' tunnelling, and is similar to the phenomenon utilized in semiconductor resonant tunnelling devices [13, 14]. In such a two-step mode of transport, the current is enhanced at potentials where it is possible for electrons to occupy the accessible state of the molecule before tunnelling out into an available electrode state. Calculations with redox-active organometallic (ferrocene and cobaltocene) molecules have previously shown that the potential forms a barrier around the HOMO of the metal centre, indicating that the centre behaves as a potential well much like a quantum dot [15, 16], trapping the electron in the molecular state.

In redox-active proteins, however, nuclear fluctuations may bring the molecular levels into resonance with electrode DOS and in this case the two steps may occur only at favourable nuclear configurations. This process is called two-step redox-assisted tunnelling to distinguish it from the quantum well description previously mentioned, closely aligned to electrochemical theories. The major difference between these two 'two-step' modes is the required involvement of nuclear motion in the redox-assisted case. Using arguments based on Marcus theory, Sumi *et al* have calculated the tip–substrate current–voltage relationship in an STM configuration considering transport purely through a redox-protein's active centre [17].

In an alternative model where tunnelling can be gated, at specific voltages the barrier height is lowered due to a more efficient pathway for electron transfer being presented. The electrons tunnel coherently between the electrodes without necessarily reducing the molecule [18], so the process may be referred to as a 'one-step' mechanism. This disregards the need for thermal activation as the potential barriers are sufficiently low or short such that direct tunnelling is an effective means of transport, i.e. tunnelling probability is close to one and the regime is adiabatic.

In addition to the enhanced (gated) conductance available at specific voltages in redox systems transmission theory also predicts the possibility of negative differential resistance (NDR), where increasing the bias voltage leads to a decrease in current. Specifically, in calculations of currents in resonant tunnelling metal–molecule–metal junctions, a peak in the DOS present in either electrode will lead to an enhancement of current when the redox state and the electrode states overlap. This is possible when there is a sharp tip [19] or even when the 'tip' is treated as a planar arrangement of metal atoms [15]. When the DOS peak passes the molecular level there is a corresponding drop in current, resulting in NDR.

NDR has been observed in the I–V spectra of YCC using CP-AFM (see section 3). In order to predict and calculate NDR in I–V curves using the above models of resonant electron transport it is necessary to calculate overlap of DOS in the tip–molecule–substrate system to suitable degree of accuracy. This is possible for small organic molecules at low temperatures [15, 16] but for relatively large redox systems at room temperature complexity is prohibitive. In an effort to provide a simple yet informative picture of resonant tunnelling, we implement here a modified form of the Simmons model (equation (1)) in which the effects of resonance are simulated by allowing the tunnel barrier height ϕ to dip at appropriate potentials (and to rise again as DOS move out of resonance, figure 1). The form of the dip is arbitrarily chosen to be Gaussian:

$$\phi(V) = \phi_0 - \phi_{\text{red}}\frac{1}{\sigma\sqrt{2\pi}}\exp\left(\frac{-(V - V_{\text{r}})}{2\sigma^2}\right) \quad (3)$$

where ϕ_0 is the constant barrier height away from resonance, ϕ_{red} is a prefactor determining the reduction in height, V_{r} the resonance voltage in eV and σ specifies the full width at half maximum (FWHM $\approx 2.35\sigma$) of the depression.

The model can be used to fit observed data obtained in YCC molecular tunnelling junctions. A least squares minimization method is used and the initial parameters are set by the peak–valley distance in bias for σ, the peak position for V_{r} and $\phi_{\text{red}} = 0.1$. The barrier length is fitted and assumed to be constant across the bias range. It can be seen from figures 1 and 2 that this Gaussian form fits the observed current maxima well and is typical of the majority of I–V sweeps that demonstrate NDR. The fitted decrease in barrier height provides insight into the change observed at resonance.

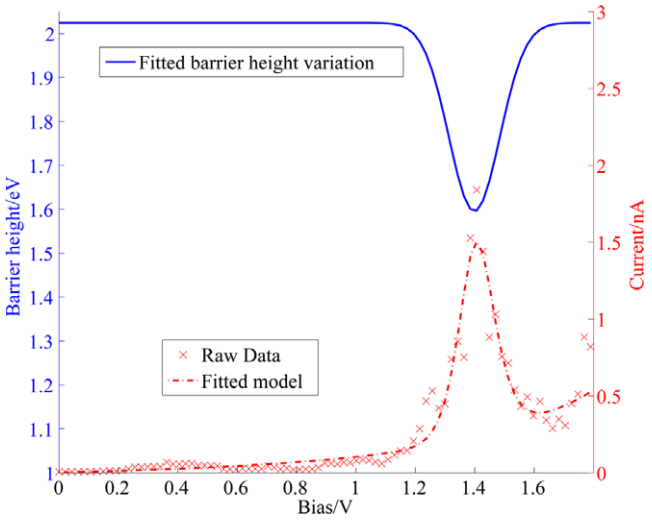

Figure 1. Left axis: example of variation of barrier height with bias in the modified Simmons model. The form of the dip is Gaussian. Right axis: the fitted I–V curve with original unfiltered data for a YCC CP-AFM junction. This sweep was taken at 2.2 nN with a Pt-coated tip in an nitrogen atmosphere.

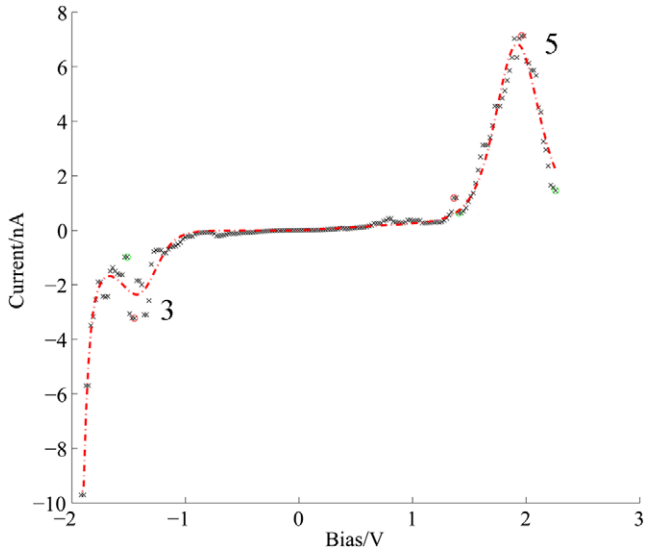

Figure 2. An example of the variable barrier height model fitted using the least squares approach to positive and negative peaks on the same I–V sweep in a CP-AFM YCC junction at 3 nN load. The labels at each peak give the PV ratio for that maximum. The maxima occur between 1 and 2 V but are typically asymmetric in both position and magnitude. At negative bias the preamplifier has saturated at ∼−2 V. Fitting to the large peak at positive bias tracks the data closely; at negative bias the fit is not as good due to the noisier nature of this current maximum. While median filtering of the data may aid fitting this could obscure potentially interesting current spikes and so the raw data is used.

Figure 1 demonstrates a maximum drop in effective barrier height of 20%, a considerable reduction. The accuracy with which the model tracks measured data indicates that a coherent tunnelling mechanism may still be dominant in these molecular junctions even at resonance. It is possible that another transport mechanism such as coherent two-step tunnelling [20] or two-step hopping [21] is the physical process at resonance; the drop in the 'apparent' one-step barrier height does not necessarily specify any one mechanism, though the effect is to reduce the barrier height as if the mechanism were one-step. Further to this, it is most probable from the form and magnitude of the measured currents (i.e. sigmoidal increase and appreciable tunnelling current) that the off resonance mechanism is indeed direct in the 3–10 nN load range, as it is at higher loads across the bias range.

2. Experimental methods

Yeast iso-1-cytochrome c (*Saccharomyces cerevisiae*), purchased from Sigma, was used as received. Monolayers of the protein were formed on high-purity gold substrates (Arrandee), which were sonically cleaned in deionized water and annealed in a butane flame for several minutes to form atomically flat terraces. A 100 μM solution of YCC (40 mM PBS buffer, pH 7.0) was reduced with TCEP disulphide reducing gel (Pierce) for at least half an hour with occasional stirring, after which the supernatant liquid was removed and diluted to 1–10 μM YCC. The freshly annealed gold was allowed to cool before being submerged in the protein solution and incubated overnight at 4 °C. The surface was rinsed copiously with deionized water and dried under a nitrogen stream before mounting on the SPM platform. Zn-azurin was kindly supplied by Professor Gerard Canters, Dept Chemistry, University of Leiden, Netherlands. Zn-azurin layers were formed in the same manner as YCC but without the need for reduction with TCEP gel (the surface disulphide is readily accessible [9]). CP-AFM and EC-STM measurements were performed using a PicoSPM (Molecular Imaging Inc.) system. CP-AFM was performed in 'ambient' operation, with the environmental chamber of the AFM was filled with nitrogen to reduce the humidity to ∼20%. Platinum-coated AFM probes (∼2 N m^{-1}, Mikromasch) were used to engage the protein surface at minimal force (∼1 nN), after which the applied load was incrementally increased. Bias sweeps were taken over 0.5 s in both the upward and downward directions. Fitting of the low-bias linear resistance and the medium-voltage Simmons model was achieved by a program written in-house in Matlab, as was automated detection of I–V maxima and measurement of peak–valley current ratios of such spikes. EC-STM imaging and *in situ* cyclic voltammetry were performed under buffer solution with Ag pseudoreference and Pt counter electrodes. Gold STM tips were etched in a 1:1 solution of HCl and ethanol at 2.4 V and then coated with apiezon wax. Prior to use the EC-STM fluid cell and Pt counter electrode were cleaned with piranha (3:1 H_2SO_4:H_2O_2). Additional adlayer characterization was carried out using ellipsometry and surface plasmon resonance (SPR, Autolab).

3. Results and discussion

3.1. Protein adlayer characterization

The protein SAMs were characterized by contact-mode AFM (imaging force 2–4 nN) in deionized water to elucidate coverage and homogeneity, and to estimate layer thickness.

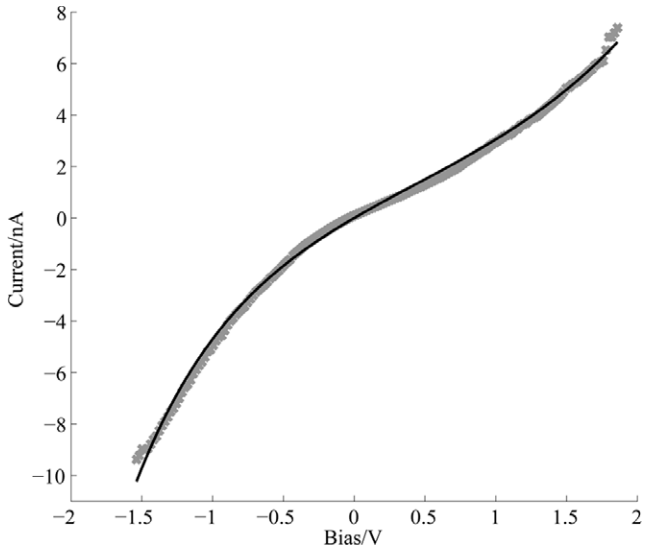

Figure 3. An example of the fitting of the Simmons model to I–V data taken on YCC at 40 nN applied load with a platinum-coated AFM tip. The raw data is denoted by grey crosses, with the solid black line showing the fitted Simmons model, $L = 0.75$ nm, $\phi = 3.3$ eV.

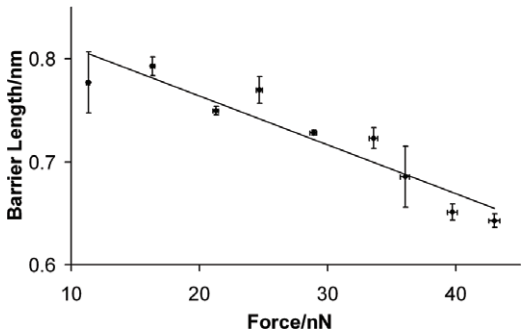

Figure 4. Variation of CP-AFM tunnelling barrier length with force for YCC adsorbed on bare gold as measured by Simmons fitting for forces over 10 nN. The tunnelling area was taken to be a circle of radius determined using the Hertz model. Error bars in length are the standard deviation of all sweeps at one force, while the force error bars are derived from the scatter of measured forces. Fitted line $L = -0.005F + 0.9$, where the gradient can be related to the Young's modulus of the molecular layer.

Lithographic removal of protein was carried out at a force of ∼40 nN, high enough to remove adsorbed molecules but not sufficient to dig into the underlying substrate. An increase in scan size, imaging and cross sectional analysis at minimal load (2 nN) leads to a thickness elucidation of 3–4 nm. This value is well aligned with layer thicknesses as measured by ellipsometry, and lies within 10% of the crystallographic molecular dimensions. SPR demonstrated coverages of ∼100%, consistent with the AFM imaging and ellipsometry measurements.

3.2. Barrier length modulation at high applied loads using CP-AFM

Current–voltage data was observed to fall into three regimes according to probe force. The minimum load at which electrical contact is stable is ∼3 nN. At forces exceeding 10 nN I–V spectra are smooth and show monotonically increasing current with bias. This contact regime can be used to elucidate the effect of the perturbative force from the probe on the sample. The Simmons model of equation (1) is fitted to obtain an estimate of the barrier length and height (figure 3). This fitting assumes a circular tunnelling area, which is the multiplier of the current density in equation (1) quantifying the total current through the junction. While it is possible to use a nominal assumed area (as this term lies outside of the exponential function), we increase the calculated barrier length accuracy by deriving a tunnelling area from a Hertzian model for elastic contact of the tip and protein layer [22]. The Young's modulus of the protein is required for this calculation and was itself derived from the variation of barrier length with an initially assumed tunnelling area equivalent to that presented by one YCC molecule (10 nm^2). While this is designed to provide a more accurate estimate of barrier length and height, we observe that the qualitative behaviour of the Simmons fitting parameters is very similar if the nominal 1.8 nm radius is taken, and measured barrier lengths differ by less than 10% at any one load. The contact areas also provide an estimate of the number of molecules residing in any one tip–protein–substrate junction; the largest contact radius predicted across this spread of force equates to 5 molecules or less. This is a number sufficiently low to resolve individual molecule contributions.

Between 30 and 70 I–V sweeps were fitted and the results averaged for any given applied load. The sweep direction was toggled between upwards and downwards for successive sweeps. If both the barrier length and height are fitted along with the asymmetry factor then a decreasing trend in the barrier length from 0.77 to 0.59 nm over the 11–43 nN force range is observed, in line with observations in other studies [2–4, 23]. If the barrier height is maintained at the mean of those measured (it shows a flat profile across the 11–43 nN force range), and the curve is subsequently fit again with only the height and asymmetry factor as free fitting parameters then a linear downward trend in barrier length is observed with less scatter (figure 4). Heuristically this will lead to an exponential decrease in low-bias molecular resistance since, near zero bias, $I \propto V\mathrm{e}^{-\beta L}$. This trend is observed (figure 5) with resistances varying from ∼36 GΩ at 11 nN load to ∼0.34 GΩ at 43 nN. Since significant molecular compression is expected in the 5–10 nN force regime, a simple linear extrapolation of barrier length to zero force (which predicts an 'unperturbed' length of ∼0.9 nm) is expected to underestimate the uncompressed protein height. While it is possible to fix the barrier height at loads >10 nN due to the observed lack of variation with force, it is expected to vary at lower loads [3], thus affecting the fitted barrier length. Observations of the barrier length trend at sub 10 nN forces are complicated by the occurrence of negative differential resistance in this regime (see below).

In summary, reliable electrical contact to chemisorbed YCC molecules can be established at loads of 3 nN and above. At forces over 10 nN current through the tip–molecule–substrate junction is observed to monotonically increase with

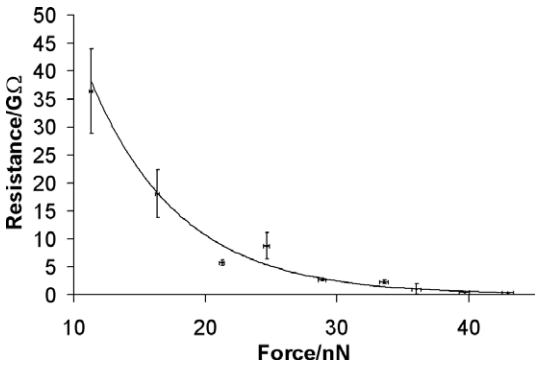

Figure 5. Variation of the low-bias resistance of YCC. Here the low-bias regime is taken to be between ±0.15 V. If the measured resistances exhibited a multimodal distribution then the values in the highest-resistance peak only were taken, as this is assumed to be the configuration that probes the fewest individual molecules. The fitted curve is exponential, as expected from the low-bias Simmons tunnelling formalism.

bias and is well described by a direct tunnelling model, fitting of which shows barrier lengths that systematically decrease with force. Junction resistance decreases exponentially with force across this regime from 36 GΩ at 11 nN to 0.34 GΩ at 40 nN.

3.3. Redox-assisted transport at low applied loads

At low applied loads of 3–10 nN the *I*–*V* spectra of YCC show distinct maxima, as shown in figures 1 and 2, in contrast to the smooth monotonically increasing currents seen at high force. In this analysis a peak is taken to have a peak-valley (PV) current ratio of >1.5, with maxima below this value attributed and dismissed as noise. Such current maxima are not detected with saturated alkyl adlayers electronically probed under equivalent conditions or the electrochemically-inactive metalloprotein Zn-azurin. In contrast, peaking is seen in all datasets on YCC in the force range 3–10 nN, with frequencies of up to 100% of sweeps at any one load[1]. The bias at which the NDR maxima are observed fluctuates widely even within datasets, with means at ∼ ±1 V and standard deviations of ∼0.5 V. This phenomenon has been observed by others in metal–redox-molecule–metal junctions [24, 25] but the reason for such a wide variation is, at present, unclear (though piezo drift and the fluctuating coupling of the thermally vibrating cantilever to the protein may be significant contributors). The NDR maxima are well described by the coherent tunnelling model described in section 1.1 (figures 1 and 2), and so it is postulated that a one-step resonance mechanism is the dominant method of charge transport for these junctions. The presence of distinct maxima indicate that there are sharp features present in the tip or substrate electronic DOS. It should be noted that it is possible that NDR is caused by a physical change in protein structure due to the large applied field at high biases. However, recent EC-STM *I*–*V* data demonstrate that the position of the NDR resonance is electrochemically gateable (manuscript in preparation), confirming its origin in redox chemistry.

In considering the equivalence between low-force CP-AFM tunnel junctions and those generated in an EC-STM configuration at low tunnel set point, where, in both cases, tip–molecule electronic coupling is likely to be weak (and redox-assisted transport accordingly more significant) we have carried out analyses of protein junctions under electrolyte. Under such conditions it is possible to definitively assign the role of the metal redox site.

3.4. Electrochemically-induced conductance modulation using EC-STM

3.4.1. YCC. In the CP-AFM experimental configuration used above the potential of the tip is kept at virtual ground with the substrate potential swept across the desired bias range; it is not possible to control the tip/substrate potential relative to a reference due to the practical difficulties in the required coating of conductive cantilevers under electrolyte (although this is an active area of research [26–31]). The EC-STM modality permits full electrochemical control by locking potentials to a reference point. *In situ* high resolution EC-STM images of YCC molecules on bare gold (figure 6(A)) were acquired in phosphate-buffered saline, pH 7.5. Though STM-derived height data is a convolution of topographic and electronic contributions, its analysis can be a useful means of tracing conductance change (figure 6(B)). By performing STM imaging under electrochemical control it is possible to tune the electrochemical potential of the working electrodes (substrate and tip) to the protein redox midpoint potential [32–34], allowing an investigation of the coupling between redox events and image contrast (figure 6(B)).

Figure 6(C) shows a typical *in situ* cyclic voltammogram of YCC adsorbed on a bare gold surface. The equilibrium redox potential (or half-wave potential), as measured from the CV is 320 ± 7 mV versus SHE [5, 8]. At surface potentials close to the half-wave potential (±15 mV) image contrast is maximized and falls by 3.1 ± 0.5 Å at overpotentials either side of this. The close correlation of voltammetry with gated conductance strongly supports a tunable redox contribution to tunnelling [35, 36].

3.4.2. Conductance gating in HHCC. YCC is adsorbed directly to the gold surface via its surface cysteine. In order that the effect of decoupling the protein from the planar electrode be investigated a spacing monolayer is introduced, on to which the protein is adsorbed. The increased protein–electrode tunnelling distance will retard the electron transfer rate [37] and is expected to lead to a lower observed effect of substrate potential on image contrast. HHCC and YCC are structurally similar except for the absence of a surface cysteine residue in HHCC; rather than being directly chemisorbed to

[1] While the Zn-azurin control demonstrates no NDR at loads above 3 nN, some peaks are seen at forces below this value. However, the PV ratio of these indicates that their origin in spurious noise rather than any molecule-specific phenomenon. The mean largest PV ratio for YCC at any given force is 39.2, compared to 7.9 for Zn-azurin at loads lower than 3 nN, five times lower than the YCC average. The highest PV measured for YCC was 109.6, compared to 13.3 for the control (note that preamp saturation at 10 nA may obscure higher amplification).

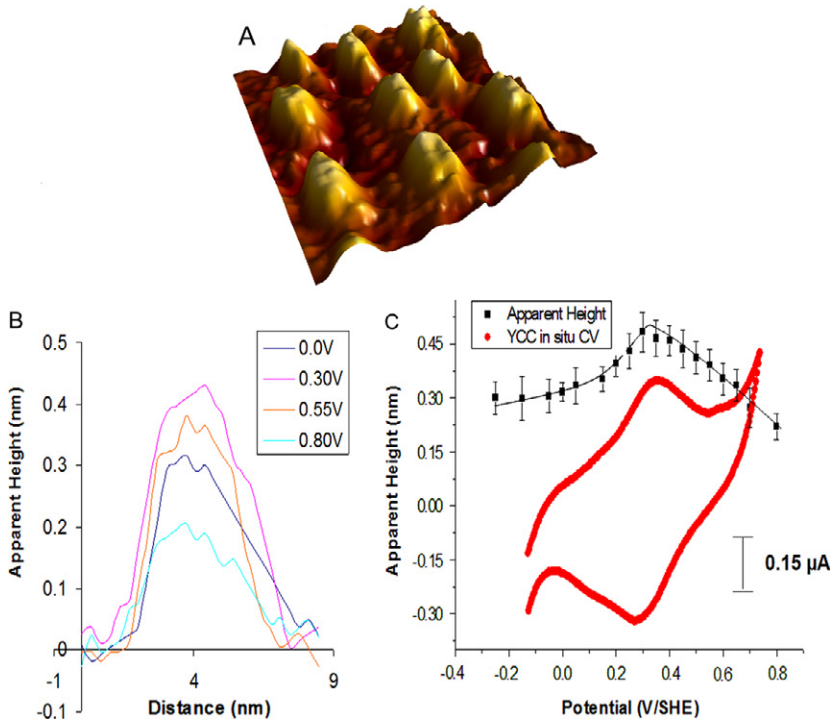

Figure 6. (A) *In situ* electrochemical STM image of YCC molecules adsorbed onto a pristine gold electrode surface in 10 mM phosphate buffer, pH 7.5. 25 nm × 25 nm, Z range 6 Å. Constant-current mode; working electrode potential 300 mV/SHE, tip bias −300 mV, tunnelling current 300 pA. Each molecule is approximately 3 nm in diameter and contains one redox-addressable heme group. The latter plays a role in 'gating' molecular conductance electrochemically in mediating tunnelling, under appropriate experimental conditions. (B) Single molecule cross section profile of one molecule showing the STM-derived height of a YCC molecule adsorbed on Au(111) at varying substrate potentials. (C) Averaged apparent height of more than 20 molecules as a function of the substrate potential, and *in situ* cyclic voltammogram of the YCC monolayer. The apparent height is greatest at the electrochemical half-wave potential.

the surface the protein is held in place electrostatically by using a suitable terminal functionality on an alkanethiolate monolayer. Due to the charge distribution on the surface of the protein this method also orients the protein in a favourable configuration for electron transport [37]. Using Laviron's method the electron transfer rate constant k_{et} for HHCC is calculated to be 10 ± 1 s^{-1}, while k_{et} for YCC on bare gold is reported to be as high as 1774 s^{-1} [5]. Figure 7(A) is a tunnelling image of HHCC molecules electrostatically self-assembled on a 11-mercaptoundecanoic acid SAM in electrochemically-addressable arrays. A typical CV of this surface is given in figure 7(C). As with YCC, the apparent height of molecular features for HHCC was measured at varying substrate potentials. Figure 7(C) shows that the apparent molecular height can increase by up to ∼2.0 Å with a mean of 1.2 ± 0.4 Å, 61% less than the mean figure obtained for YCC, and shows a clear maximum around the equilibrium potential of HHCC. Though the molecular conductance is clearly electrochemically gated, the presence of the spacing monolayer and the reduced molecule–electrode electronic coupling thus generated appears to reduce the impact of electrode Fermi alignment with redox-based DOS.

3.4.3. Quantification of protein conductance modulation. As discussed earlier, the presence of accessible electronic states in the redox-active protein leads to the possibility of resonant tunnelling through the system. Alternative models of transport describe the tunnelling proceeding in one or two steps. NDR maxima have been successfully described by a coherent one-step model that utilizes a change in the barrier height to capture the characteristics of the resonance. Similarly, to relate the observed molecular height change in the EC-STM configuration, Δh_{STM}, with a conductance change in the protein itself, it is again assumed that transport occurs in one coherent step. As with the discussion of NDR in the CP-AFM junction above this is intended to be a practical description of protein conductance change, as opposed to a comment on the actual transport mechanism.

At the high tunnel junction transimpedances used for imaging these layers, the tip is expected to be positioned physically above the molecules, a model supported by the nondestructive imaging of the sample over long time periods. This results in a tunnel junction composed of two distinct layers (figure 8): the protein, with a height h_P and a transconductance, G_P, and the tip–layer gap with adjustable transconductance determined by the separation, d_g, controlled by the imaging feedback loop. The constant-current STM topograph is a surface of constant tunnelling current with contributions from both the protein layer and the tip–protein gap $h_{STM} = h_P + d_g$ (note that Δh_{STM} at differing substrate potentials is measured, not h_{STM} directly). From this, an analysis of imaging profiles facilitates a quantification of conductance change. The transconductances, G, across each

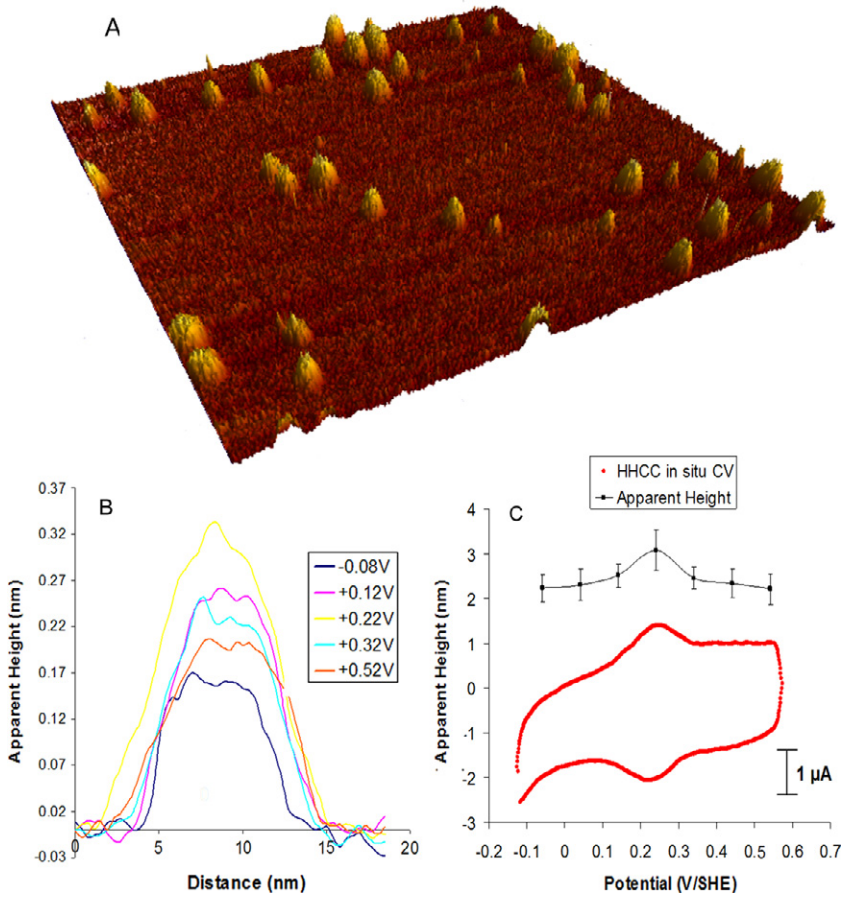

Figure 7. (A) EC-STM image of HHCC adsorbed on 11-mercaptoundecanoic acid SAM in 22 mM phosphate buffer, pH 7.01. 200×200 nm^2, Z range 0.4 nm. Tunnelling current 80 pA, tip bias 100 mV, substrate potential at the midpoint potential of 222 mV/SHE. (B) Single molecule cross section profile of one molecule in (A) at varying substrate potential. (C) Averaged apparent height of more than 20 molecules as a function of the substrate potential, and *in situ* cyclic voltammogram of the HHCC monolayer. The apparent height is greatest at the electrochemical half-wave potential of HHCC.

layer are

$$G_g = A \exp(-\alpha d_g) \tag{4}$$

and

$$G_P = B \exp(-\beta h_P) \tag{5}$$

for the tip–sample gap and protein respectively, where α and β are the respective decay constants, and the prefactors, A and B, are the respective contact conductances. Because the transconductance is an electron tunnelling probability, as opposed to a dissipative current flow (in a bulk conductor, for example), the transconductance of the composite two-layer tunnel junction, G_t, is the product of the transconductances of the component layers:

$$G_t = G_g G_P. \tag{6}$$

The STM operating with constant-current feedback constrains G_t to be constant over the image:

$$\begin{aligned} G_t &= G_{g1} G_{P1} = G_{g2} G_{P2} = i_t/e_t = \text{constant} \\ \therefore \frac{G_{P2}}{G_{P1}} &= \frac{G_{g1}}{G_{g2}} = \exp(-\alpha_1 h_{g1}) \exp(\alpha_2 h_{g2}) \\ \therefore \frac{G_{P2}}{G_{P1}} &= \exp(-\alpha \Delta h_{STM}) \end{aligned} \tag{7}$$

where e_t is the tunnel junction bias voltage and i_t is the tunnelling set point. Here the simplifying and reasonable assumption that the characteristics of the buffer gap do not change significantly at different substrate potentials ($\alpha_1 \sim \alpha_2$, $A_1 \sim A_2$) has been employed. The decay constant of the buffer solution can be estimated to be close to 1 Å^{-1} [38], and so if Δh_{STM} is measured in ångströms then the ratio of protein conductances is

$$\frac{G_{P2}}{G_{P1}} = \exp(-\Delta h_{STM}). \tag{8}$$

The increase in STM apparent height of 3.1 ± 0.5 Å for YCC therefore corresponds to an increase in protein junction conductance of some 22-fold. This value is comparable with the conductance increases seen in small redox-active molecules such as bipyridinium and protoporphyrins [39–41] and wild type azurin on alkanethiol SAMs [42] for which electronic k_{et} is expected to be high. The ~1.2 Å mean height increase for HHCC likewise corresponds to a 3.4-fold conductance enhancement and presumably reflects the increased redox site electrode spacing (i.e. decreased electronic coupling) [43]. The effects of resonance on molecular conductance should scale with the degree of electrode–molecule coupling.

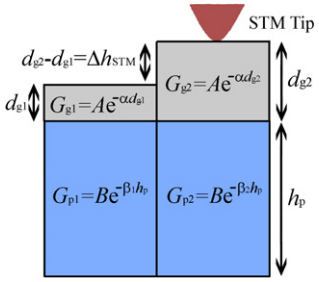

Figure 8. Schematic of the two-layer tunnelling model used to estimate the change in protein conductance between on and off resonance potentials. Parameters are as defined in the text.

If one assumes that the bias range of nondestructive imaging corresponds to the non-adiabatic regime, then the enhancements observed here are broadly as expected [21]. The results presented here represent a preliminary investigation and the modulation of molecular conductance is subject to further experimental analysis. These observations not only appear to align observations in low-force CP-AFM junctions to those observed in the EC-STM configuration but also reinforce the importance of electrode–molecule electronic coupling on both conduction mechanism and ones ability to gate. In this work, we measure the conductance maximum to be close to the electrochemical midpoint potential of the protein. Previous theoretical treatments have predicted an offset in the conductance maximum from the midpoint potential equal to the reorganization energy λ of the protein (for biases near zero) if the electron transport mechanism is two-step coherent [20]. Such an offset is also expected for a one-step coherent process. For a two-step process with full relaxation the conductance peak would be close to zero for biases near zero and would be offset by any applied bias [21]. In the tip–substrate gap redox-based reorganization energies are expected to be reduced from those measured in fluid since spatial constriction reduces solvent access and its contribution to the total reorganization. Terrettaz *et al* [44] measure λ to be $\sim$0.6 eV for a variety of c-type cytochromes in solution. It is, accordingly, feasible that, within the confines of a tunnelling junction where the protein is tethered to one electrode and constricted by the other, the reorganization energy is much lower than this. The offset will, then, be accordingly small. In considering the ability of this measured offset to diagnose the electron transport mechanism, then, it is important to note both that LUMO-based tunnelling should be associated with the conductance maximum moving towards the midpoint potential as bias is increased and that the effects of bias on this offset will depend on the electron transport mechanism [21, 45]. It is not possible to rule out the possibility that the bias values utilized in this study are sufficient to mask any offset and it is, accordingly, our current view that the combined effects of (probable) low reorganization and unknown bias dependence make the conclusion of a definitive electron transport mechanism (based on the peak offset from the electrochemical midpoint) difficult.

4. Conclusions

In the establishment of robust mechanical contact between a compressional metalloprotein and a proximal probe contact, transport across the junction is well described by a nonresonant tunnelling model where barrier lengths and junction resistances vary linearly and exponentially respectively with calibrated force. Junction resistance is reduced from $\sim$36 GΩ at 11 nN load to $\sim$0.34 GΩ at 43 nN. On decreasing the coupling between the AFM probe and the molecule, direct, nonresonant tunnelling becomes considerably less facile and is swamped by the onset of current surge at specific bias. This negative differential resistance, not observed in non-redox-active proteins to a statistically comparable degree, is ascribed to the onset of resonance and is well described by a coherent tunnelling model in which the barrier height is gateable through substrate potential. We have sought to equate the weakly coupled CP-AFM junctions with low tunnel set point EC-STM junctions where probe–molecule coupling is expected to be equivalently weak. Observations of redox-assisted NDR in the former are mirrored by resonant conductance under electrolyte in the latter, where molecular conductance is potentiostatically gateable across more than an order of magnitude in proteins robustly coupled to the underlying electrode. On decreasing the electronic coupling between a structurally equivalent cytochrome and the planar electrode, through the use of a spacer SAM, the magnitude of conductance switching is significantly lower. Though preliminary, this may indicate that conductance switching magnitude scales with and is maximized by strong electrode–redox site coupling (with corresponding high electrochemical k_{et}). As with the NDR regime of CP-AFM junctions, a coherent tunnelling model, where alignment of the substrate potential with the electrochemical half-wave potential leads to barrier indentation, is utilized to describe the conductance change on gating in an EC-STM configuration. For the directly chemisorbed cytochrome, where electrochemical coupling to the underlying substrate is robust, molecular conductance is 22-fold greater at resonance than off. For HHCC, decoupled from the gating electrode, conductance changes are reduced to $\sim$3 fold.

References

[1] Zhao J and Davis J J 2003 Force dependent metalloprotein conductance by conducting atomic force microscopy *Nanotechnology* **14** 1023–8
[2] Zhao J and Davis J J 2005 Molecular electron transfer of protein junctions characterised by conducting atomic force microscopy *Colloids Surf.* B **40** 189–94
[3] Zhao J, Davis J J, Sansom M S P and Hung A 2004 Exploring the electronic and mechanical properties of protein using conducting atomic force microscopy *J. Am. Chem. Soc.* **126** 5601–9
[4] Axford D, Davis J J, Wang N, Wang D, Zhang T, Zhao J and Peters B 2007 Molecularly resolved protein electromechanical properties *J. Phys. Chem.* B **111** 9062–8
[5] Heering H A, Wiertz F G M, Dekker C and de Vries S 2004 Direct immobilization of native yeast iso-1 cytochrome c on bare gold: fast electron relay to redox enzymes and zeptomole protein-film voltammetry *J. Am. Chem. Soc.* **126** 11103–12

[6] Szucs A and Novak M 1995 Stable and reversible electrochemistry of cytochrome c on bare electrodes part II: Effect of experimental conditions *J. Electroanal. Chem.* **384** 47–55

[7] Hansen A G, Bolsen A, Nielsen J U, Wackerbarth H, Chorkendorff I, Andersen J E T, Zhang J and Ulstrup J 2003 Adsorption and interfacial electron transfer of *Saccharomyces cerevisiae* yeast cytochrome c monolayers on Au(111) electrodes *Langmuir* **19** 3419–27

[8] Bonanni B, Alliata D, Bizzarri A R and Cannistraro S 2003 Topological and electron-transfer properties of yeast cytochrome c adsorbed on bare gold electrodes *ChemPhysChem* **4** 1183–8

[9] Alessandrini A, Gerunda M, Canters G W, Verbeet M P and Facci P 2003 Electron tunnelling through azurin is mediated by the active site Cu ion *Chem. Phys. Lett.* **376** 625–30

[10] Chien J C W 1978 Effect of metal substitution on the molecular structures and functional properties of cytochrome c and hemoglobin *J. Phys. Chem.* **82** 2171

[11] Axford D N and Davis J J 2007 Electron flux through apo- and holoferritin *Nanotechnology* **18** 1–7

[12] Simmons J G 1963 Gerneralized formula for the electric tunnel effect between similar electrodes separated by a thin insulating film *J. Appl. Phys.* **34** 1793–803

[13] Sze S M 1981 *Physics of semiconductor devices* 2nd edn (New York: Wiley)

[14] Datta S 1995 Electronic transport in mesoscopic systems *Cambridge Studies in Semiconductor Physics and Microelectronic Engineering* vol 3 (Cambridge: Cambridge University Press)

[15] Wang S, Lu W, Zhao Q and Bernholc J 2006 Resonant coupling and negative differential resistance in metal/ferrocenyl alkanethiolate/STM structures *Phys. Rev.* B **74** 195430

[16] Liu R, Ke S, Baranger H U and Yang W 2006 Negative differential resistance and hysteresis through and organometalling molecule from molecular-level crossing *J. Am. Chem. Soc.* **128** 6274–5

[17] Sumi H, Hori Y and Mukai K 2006 Marcus parabola and reorganization energies associated with redox change of electron-transfer proteins detected by V–I characteristics of STM currents *J. Electroanal. Chem.* **592** 46–62

[18] Hansen A G, Zhang J, Christensen H E M, Welinder A C, Wackerbarth H and Ulstrup J 2004 Electron transfer and redox metalloenzyme catalysis at the single-molecule level *Isr. J. Chem.* **44** 89–100

[19] Xue Y, Datta S, Hong S, Reifenberger R, Henderson J I and Kubiak C P 1999 Negative differential resistance in the scanning tunneling spectroscopy of organic molecules *Phys. Rev.* B **59** R7852–5

[20] Friis E P, Kharkats Y I, Kuznetsov A M and Ulstrup J 1998 *In situ* scanning tunneling microscopy of a redox molecule as a vibrationally coherent electronic three-level process *J. Phys. Chem.* A **102** 7851–9

[21] Albrecht T, Guckian A, Kuznetsov A M, Vos J G and Ulstrup J 2006 Mechanism of electrochemical charge transport in individual transition metal complexes *J. Am. Chem. Soc.* **128** 17132–8

[22] Schneegans O, Hounze F, Meyer R and Boyer L 1998 Study of the local electrical properties of metal surfaces using an AFM with a conducting probe *IEEE Trans. Compon. Packag. Manuf. Technol.* A **21** 76–81

[23] Davis J J, Wang N, Morgan A, Zhang T and Zhao J 2006 Metalloprotein tunnel junctions: Compressional modulation of barrier height and transport mechanism *Faraday Discuss.* **131** 167–79

[24] Gorman C B, Carroll R L and Fuierer R R 2001 Negative differential resistance in patterned electroactive self-assembled monolayers *Langmuir* **17** 6923–30

[25] He J and Lindsay S M 2005 On the mechanism of negative differential resistance in ferrocenylundecanethiol self-assembled monolayers *J. Am. Chem. Soc.* **127** 11932–3

[26] Macpherson J V and Unwin P R 2000 Combined scanning electrochemical-atomic force microscopy *Anal. Chem.* **72** 276–85

[27] Kranz C, Kueng A, Lugstein A, Bertagnolli E and Mizaikoff B 2004 Mapping of enzyme activity by detection of enzymatic products during AFM imaging with integrated SECM–AFM probes *Ultramicroscopy* **100** 127–34

[28] Patil A, Sippel J, Martin G W and Rinzler A G 2004 Enhanced functionality of nanotube atomic force microscopy tips by polymer coating *Nano Lett.* **4** 303–8

[29] Frederix P L T M, Gullo M R, Akiyama T, Tonin A, de Rooij N F, Staufer U and Engel A 2005 Assessment of insulated conductive cantilevers for biology and electrochemistry *Nanotechnology* **16** 997–1005

[30] Patil A V, Vlijm R and Oosterkamp T 2006 Polymer coated carbon nanotube probes for scanning electrochemical microscopy *NSTI Nanotechnology Conf. and Trade Show (Boston, MA, 2006)*

[31] Gullo M R, Frederix P L T M, Aklyama T, Engel T, deRooij N F and Staufer U 2006 Characterization of microfabricated probes for combined atomic force and high-resolution scanning electrical microscopy *Anal. Chem.* **78** 5436–42

[32] Friis E P, Andersen J E T, Kharkats Y I, Kuznetsov A M, Nichols R J, Zhang J and Ulstrup J 1999 An approach to long-range electron transfer mechanisms in metalloproteins: *In situ* scanning tunneling microscopy with submolecular resolution *Proc. Natl Acad. Sci. USA* **96** 1379–84

[33] Davis J J, Hill H A O and Bond A M 2000 The application of electrochemical scanning probe microscopy to the interpretation of metalloprotein voltammetry *Coord. Chem. Rev.* **200–202** 411–42

[34] Facci P, Alliata D and Cannistraro S 2001 Potential-induced resonant tunneling through a redox metalloprotein investigated by electrochemical scanning probe microscopy *Ultramicroscopy* **89** 291–8

[35] Schmickler W 1990 On the possibility of measuring the adsorbate density of states with a scanning tunneling microscope *J. Electroanal. Chem. Interfacial Electrochem.* **296** 283–9

[36] Kuznetsov A M, Somner-Larsen P and Ulstrup J 1992 Resonance and environmental fluctuation effects in STM currents through large adsorbed molecules *Surf. Sci.* **275** 52–64

[37] Song S, Clark R A, Bowden E F and Tarlov M J 1993 Characterization of cytochrome c/alkanethiolate structures prepared by self-assembly on gold *J. Phys. Chem.* **97** 6564–72

[38] Hahn J R, Hong Y A and Kang H 1998 Electron tunneling across an interfacial water layer inside an STM junction: tunneling distance, barrier height and water polarization effect *Appl. Phys.* A **66** S467

[39] Gittins D I, Bethell D, Schiffrin D J and Nichols R J 2000 A nanometer-scale electronic switch consisting of a metal cluster and redox-addressable groups *Nature* **408** 67–9

[40] Tao N J 1996 Probing potential-tuned resonant tunneling through redox molecules with scanning tunneling microscopy *Phys. Rev. Lett.* **76** 4066–9

[41] Haiss W, Zalinge H, Higgins S J, Bethell D, Hobenreich H, Schriffin D J and Nichols R J 2003 Redox state dependence of single molecule conductivity *J. Am. Chem. Soc.* **125** 15294–5

[42] Chi Q, Zhang J, Jensen P S, Christensen H E M and Ulstrup J 2006 Long-range interfacial electron transfer of metalloproteins based on molecular wiring assemblies *Faraday Discuss.* **131** 181–95

[43] A S Haas, Pilloud D L, Reddy K S, Babcock G T, Moser C C, Blasie J K and Dutton P L 2001 Cytochrome c and cytochrome c oxidase: Monolayer assemblies and catalysis *J. Phys. Chem.* B **105** 11351–62

[44] Terrettaz S, Cheng J and Miller C J 1996 Kinetic parameters for cytochrome c via insulated electrode voltammetry *J. Am. Chem. Soc.* **118** 7857–8

[45] Alessandrini A, Salemo M, Frabboni F and Facci P 2005 Single-metalloprotein wet biotransistor *Appl. Phys. Lett.* **86** 133902